Effect of Lattice Orientation, Surface Modulation, and Applied Fields on Free-Surface Domain Microstructure in Ferroelectrics

Lun Yang[*] and Kaushik Dayal[†]

Civil and Environmental Engineering, Carnegie Mellon University

July 6, 2011

Abstract

Ferroelectric perovskites are used in various transducer, memory and optical applications due to their attractive electromechanical and optical properties. In these applications, the ferroelectrics often have complex geometries with a significant portion of the surface free and unshielded by electrodes. The free surfaces play an important role in determining microstructure due to the intricate balance between preferred polarization orientation, mechanical stresses, and stray electric fields that exist outside the specimen. In addition, the stray electric fields at free surfaces are exploited for photochemical reactions and self-assembly. Hence, it is important to predict the domain patterns, stray fields, and mechanical stresses that form in these geometries. We apply a phase-field model in combination with finite element and boundary element methods for real-space calculations of microstructure at free-surfaces in ferroelectrics. A key advantage of the boundary element method is that it enables us to calculate the stray electric fields outside the specimen. We examine the effect of lattice orientation, surface modulation and applied far-field stress and electric field on domain microstructure and stray electric fields.

Keywords: Ferroelectric; Phase-field simulation; Free surfaces; Microstructure; Boundary element method

1   Introduction

Ferroelectric materials are widely used in sensors and actuators [1, 2]. More recently, they have found applications in high-speed memories [3], and have been proposed as elements of microwave circuits [4] and as photonic switches at small length scales [5]. A more recent application exploits the stray electric fields that appear on un-electroded ferroelectric surface as a means for templated self-assembly and to drive photochemical reactions [6, 7]. All of these applications share the feature that geometries and boundary conditions are complex and real-space methods are required. A particular geometry that

[*]luny@andrew.cmu.edu

[†]kaushik@cmu.edu

1

appears in all these settings is that of a ferroelectric free surface. For instance, many of the devices mentioned above use thin-film geometries and free surfaces play a dominant role in determining their behavior [8]. In addition, when cracks form, predicting the domain patterns on crack faces requires an understanding of the behavior at free surfaces. In the examples of self-assembly and chemical reactions, polarization being oriented normal to the free surface leads to surface charges and consequent stray fields that are central to the applications. Hence, understanding microstructure, stress, and stray electric fields at free surfaces is important for reliability, functionality and design of ferroelectric devices.

While complex geometries require real-space techniques, a central challenge is dealing with stray electric fields in this setting. These fields are long-range and exist over all space and not just within the specimen. It is important to accurately obtain the energy in these fields as it contributes to the balance between electrostatic energy, mechanical energy, and energy for the polarization to deviate from the preferred states. Hence, it plays a significant role in determining domain patterns as well as stress. In this work, we apply a recent real-space formulation that can handle these complexities [9]. In particular, our method exploits a boundary element method that enables efficient and accurate calculation of electric fields within the ferroelectric as well as the stray fields outside. We apply this to free-surface geometries and examine the domain patterns and stray electric fields. We examine the effect the relative orientation of the free surface with respect to the crystal axes, the effect of surface modulations, and the effect of applied normal stress parallel to the free surface, and applied electric fields parallel to the free surface. Instances where different relative orientations can arise include due to deposition strategies, or due to crack face orientations. Surface modulations can also appear for the same reasons. The applied fields can arise in thin-films, for instance by straining the substrate, and they lead to significant changes in stray fields and domain patterns. They can also arise due to stress concentrations such as crack tips, though here we focus on far-field applied stresses that are uniform at the scale of computation.

Ferroelectric thin-films have received much attention from first-principles calculations, e.g. [11, 12, 13, 14]. First principle calculations typically focus on extremely thin films and are restricted to zero temperature. In combination with the method of effective Hamiltonians, they have been used to examine domain patterns at finite temperature. They have provided much insight into the detailed properties near the free surface and the scale of resolution is at the (sub-) atomic scale. While these methods provide valuable understanding of ultra thin-films and the free surface, in particular issues such as possible supression of ferroelectricity in extremely thin films, they are too computationally demanding for microstructure that forms at larger scales. In addition, due to issues related to setting up the surface terminations, these have all examined films with the crystal axis oriented along the plane of the film.

The main tool of choice in understanding domain microstructure in ferroelectric thin-films is the phase-field approach. It enables the study of much larger specimens than first-principle calculations. It has been widely used to examine various aspects of ferroelectric microstructure in thin films, e.g. reviewed in [15, 16]. These aspects include, e.g., the effect of substrate constraint on microstructure [17], the related effect of strain-tuning on ferroelectric properties [18], the interplay between stress and transformation temperature [19], the role of dislocation [20], and many other questions. However, the typical electrical boundary condition, both in periodic and real-space settings, is to assume either electrodes on the surface or complete charge compensation. This assumption has the effect of completely cancellation of the stray fields outside the film and hence that contribution to the energy is not required. In [21], the authors compare complete charge compensation boundary conditions with the approximate boundary condition that electric displacement vanishes on the free surface. The latter boundary condition is essentially the approximation that stray fields are not allowed outside the body. They find interesting differences in the microstructure with these different boundary conditions, in particular, the formation of domains similar to

our results of the case when the crystal axis is parallel to the plane of the film. Here, we use the boundary condition that the normal component of the displacement is *continuous* across the free surface; this is the exact boundary condition from fundamental electromagnetism at the interface of two dielectrics, in this case ferroelectric and vacuum. Hence, this enables us to account for the stray fields outside the body.

A computational and scaling analysis of free-surface domains was provided in [9] for the relatively simple geometry when the crystal axes are oriented along the free surface. Thus, both the surface charge contribution and the anisotropy contributions favor the same polarization state (parallel to the surface). This essentially leaves a competition between mechanical energy, from the fact that the microstructure is not stress-free, and the electrostatic energy and anisotropy energy due to distortions to accommodate the microstructure. Free surface geometries are also ubiquitous in ferroelectric crack problems. However, the scale of resolution, both in theoretical and experimental studies, is typically much coarser than individual domains and averages over grains polycrystalline samples. Recent experimental efforts aimed at domain scale measurements include [22, 23] and a domain-level understanding of this process is underway [24]. We also mention phase-field studies of cracks in ferroelectrics [26, 27] including the first of a growing crack [25]; although these use approximate boundary conditions predicated on the non-existence of stray fields, they compute closure domains similar to those studied here. However, due to the geometry that is chosen for the crack, the free surface is oriented along the crystal axes. Another interesting example related to closure domains in ferroelectric rubbers appears in [28]. They make a simple ansatz for the deformation, not allowing closure, but use this to provide scaling arguments for the stray field energy to be expected when closure domains do not form.

The paper is organized as follows. We present the formulation in Section 2 and a description of the real-space method in Section 3. Section 4 describes closure domains observed at different orientations of the free surface, Section 5 describes the effect of surface modulation, Section 6 describes the effects of applied stress, and Section 7 examines the effect of applied electric field. We conclude in Section 8.

2   The Phase-field Formulation

The potential energy E of a ferroelectric body Ω (Fig. 1) with elastic strain field $\boldsymbol{\epsilon}$ and the polarization field $\boldsymbol{p}$ may be written following [29] as

$$E[\boldsymbol{\epsilon}, \boldsymbol{p}] = \int_{\Omega} \left[U(\nabla \boldsymbol{p}) + W(\boldsymbol{\epsilon}, \boldsymbol{p})\right] \, d\Omega + \frac{\epsilon_0}{2} \int_{\mathbb{R}^3} |\nabla \phi|^2 \, dV \tag{2.1}$$

where U penalizes gradients in $\boldsymbol{p}$ and models the energy contributions from domain walls, and the stored (Devonshire) energy density W penalizes $\boldsymbol{p}$ and $\boldsymbol{\epsilon}$ deviating from the spontaneous polarization and strain. The last term represents the electrostatic energy contained in the electric field $\boldsymbol{E} = -\nabla \phi$, where ϕ is electric potential obtained from Maxwell's equation:

$$\nabla \cdot (\boldsymbol{p} - \epsilon_0 \nabla \phi) = 0 \quad \text{over} \quad \mathbb{R}^3. \tag{2.2}$$

The first 2 terms in the energy (2.1) are local to the body being considered, while the electrostatic contribution is over all space.

The governing equations are obtained as a gradient flow of the potential energy [30]:

$$\mu \frac{dp_i}{dt} = \left(\frac{\partial U}{\partial p_{i,j}}\right)_{,j} - \frac{\partial W}{\partial p_i} - \phi_{,i} \quad \text{over} \quad \Omega \,, \tag{2.3a}$$

$$\left(\frac{\partial W}{\partial \varepsilon_{ij}}\right)_{,j} = 0 \quad \text{over} \quad \Omega\,, \tag{2.3b}$$

$$p_{i,i} - \epsilon_0 \phi_{,ii} = 0 \quad \text{over} \quad \mathbb{R}^3\,. \tag{2.3c}$$

The boundary conditions for the polarization evolution (2.3a) are $\nabla \boldsymbol{p} \cdot \hat{\boldsymbol{n}} = 0$, where $\hat{\boldsymbol{n}}$ is the outward normal to the boundary. Conventional elasticity boundary conditions are used for the elastic equilibrium equation (2.3b). Finally, the boundary conditions associated with Maxwell's electrostatic equation (2.3c) are potential (voltage) specified at the electrodes and decaying at infinity.

We use tetragonal barium titanate in two-dimensions as our model material, and use the same model as in [30]:

$$U(\nabla \boldsymbol{p}) = \frac{a_0}{2} \left(p_{1,1}^2 + p_{1,2}^2 + p_{2,1}^2 + p_{2,2}^2\right)\,, \tag{2.4}$$

$$W(\boldsymbol{\epsilon}, \boldsymbol{p}) = \frac{a_1}{2}\left(p_1^2 + p_2^2\right) + \frac{a_2}{4}\left(p_1^4 + p_2^4\right) + \frac{a_3}{2}p_1^2 p_2^2 + \frac{a_4}{6}\left(p_1^6 + p_2^6\right) + \frac{a_5}{4}p_1^4 p_2^4$$
$$+ \frac{1}{2}\left(\boldsymbol{\epsilon} - \boldsymbol{\epsilon}_T(\boldsymbol{p})\right) \cdot \mathbb{C} \cdot \left(\boldsymbol{\epsilon} - \boldsymbol{\epsilon}_T(\boldsymbol{p})\right)\,.$$

We also use the constants $a_0, a_1, a_2, a_3, a_4, a_5, \mathbb{C}$ and the expression for $\boldsymbol{\epsilon}_T(\boldsymbol{p})$ as in [30]. In that non-dimensionalized system, the spontaneous polarization is 1, the elastic moduli are $O(10^2)$, and the breakdown voltage across the thickness is $O(10)$.

This phase-field formulation has been widely used in real-space and periodic calculations of microstructure, e.g. [30, 9, 31, 32, 33]. Though superficially different, it is also equivalent to formulations in [34, 35, 15, 36, 37, 38, 39] to name a few.

3   Real-space Solution Technique for Stress and Stray Electric Fields

We solve the governing equations (2.3) as follows. We start with an initial polarization field that we use to obtain the strain and electric potential from (2.3bc). We then update the polarization using (2.3a). This process is repeated until convergence.

The polarization update uses a standard finite element method (FEM). We multiply (2.3a) by a test function v, integrate over the domain Ω and apply integration by parts to obtain the weak form:

$$\int_\Omega \left(\left(\frac{\partial U}{\partial p_{i,j}}\right)v_{i,j} - \frac{\partial W}{\partial p_i}v_i - \phi_{,i}v_i\right) d\Omega = \int_\Omega \mu \frac{dp_i}{dt}v_i d\Omega \tag{3.1}$$

We use standard linear triangle elements with linear shape functions to discretize $\boldsymbol{p}$. A similar approach with triangle elements and linear shape functions is used for the mechanical equilibrium equation (2.3b) with displacement as the primary variable. However, the electrostatic equation (2.3c) needs attention as the electric fields that arise on Ω are not confined to the body but extend over all space. We use a boundary element method (BEM) to resolve the electrostatic field. This enables us to efficiently solve the electric field in a finite domain (not necessarily the same as Ω) while retaining consistency with the formulation over an infinite domain. This has been described elsewhere [9, 10] and we summarize only the key points.

The electrostatic potential (2.3c) must satisfy the conditions:

$$\epsilon_0 [\![\nabla \phi(\boldsymbol{x})]\!] \cdot \boldsymbol{n} = \boldsymbol{p} \cdot \boldsymbol{n} \text{ (specified bound surface charge) on } \partial \Omega_1$$
$$\phi(\boldsymbol{x}) = V_0(\boldsymbol{x}) \text{ (specified voltage on electrodes) on } \partial \Omega_2 \tag{3.2}$$

as well as the decay conditions in the far-field. The key idea of the BEM is to consistently transform these conditions to the solution of

$$\epsilon_0 \nabla^2 \phi = \rho^* \text{ on } \Omega', \quad \phi = V_0' \text{ on } \partial\Omega' \tag{3.3}$$

This equation is readily solved with FEM with standard linear triangle elements with linear shape functions. We note that Ω' need not coincide with the specimen Ω, and by defining Ω' appropriately, we can calculate the stray electric field outside the specimen in the vicinity of the free surface. We also note that the BEM uses the Green's function for the geometry in a critical manner. Hence, in Appendix A, we present the Greens function for two-dimensions with periodicity in a single direction, as required for the geometries of interest in this paper.

We note that spectral elements [47, 16] are an alternative to finite elements to solve phase-field equations on complex geometries. However, in the current context, *neither* spectral nor finite elements are directly suitable because of the fact that electric stray fields exist over all space and the problem is posed on an unbounded domain. Once boundary elements and the Dirichlet-to-Neumann map have transformed the problem to a finite domain, then various methods, including spectral and finite elements, are applicable.

4 Effect of Relative Orientation between Crystal Axes and Free Surface

The formation of closure domains at a free surface involves a balance between anisotropy energy (that penalizes polarization and strain deviating from the crystallographically preferred states), elastic energy from stresses, and the electrostatic energy in the electric field. The electrostatic field is generated by bound bulk charges, $-\nabla \cdot \boldsymbol{p}$, as well as bound surface charges, $\boldsymbol{p} \cdot \boldsymbol{n}$. The latter contribution is particularly important at free surfaces. Minimizing this contribution, in the absence of other contributions, would align $\boldsymbol{p}$ tangential to the free surface. In previous work [9], we examined the specific case when the crystallographically preferred direction of polarization was indeed aligned with the free surface. This enabled the formation of relatively simple microstructure as both anisotropy and surface charge contributions could be minimized by the same polarization state. In this work, we examine the more complex balance that occurs when the crystal axes are not aligned with the free surface, hence forcing a competition between these contributions.

A schematic of our calculation is shown in Fig. 2. We model a ferroelectric specimen with crystal axes oriented at an angle θ to the free surface by considering a computational domain that is aligned along the free surface. We use periodicity only along the x_1 direction along the free surface, and apply far-field normal stresses and electric fields in that direction. In this section, we assume that both applied normal stress and electric field are absent but will consider them in later sections. We also assume that the body is traction free at the free surface, and can undergo only horizontal displacements on the bottom surface.

We begin from $\theta = 0$ that corresponds to the crystal axes aligned with the free surface and increase θ in discrete increments up to $\theta = 51°$. For each case, we use a domain structure of 180-domains aligned along the crystal axes but with no closure domains as the initial guess for $\boldsymbol{p}$. This domain pattern is stable in the interior but gives rise to electric fields due to the normal component of $\boldsymbol{p}$ at the free surface. The closure domains form as $\boldsymbol{p}$ and $\boldsymbol{\epsilon}$ evolve towards an energy-minimizing configuration.

When θ is small, e.g. $14°$, the closure domains that form are fairly simple and comparable to $\theta = 0$, Fig. 3(a). There is an energetic penalty as $\boldsymbol{p}$ at the surface is aligned tangentially and that is not a

crystallographically preferred state. In addition, the strain in the closure domains is not at the preferred value and this causes stresses and elastic energy. However, the electric field term dominates over these contributions and this remains the case until $\theta \simeq 27°$.

The domain patterns beyond $\theta = 27°$ are more complex. For instance, Fig. 3(b) shows the domain pattern and Fig 4(a) a detailed view of a single closure domain vector plot. At the surface, p remains horizontal so that the surface charge is absent. However, directly beneath the free surface, a new domain pattern nucleates. Some portion of this domain is aligned in the classical $90°$ closure domain pattern, while the remainder transitions from this state to a horizontally aligned state on the free surface (marked on Fig. 4(a)). This domain structure balances between the anisotropy and mechanical contributions that favor sharp domain walls with p oriented along the crystal axes, and electrical contributions that favor p aligned tangential to the free surface. The nature of this competition is also obvious in the stress and electric potential plots, Figs. 5, 6. A signature of the appearance of this new domain pattern is also evident from Fig. 9 (the stress-free curve). The electric field magnitude increases steadily until $27°$, at which point the transition domain nucleates and electric field remains fairly constant. At $37°$, the transition domain is fully developed and there is an electrical energy penalty for further increase in θ.

As we increase θ, the microstructure continues to evolve. For instance, at $\theta = 45°$, Figs. 3(c), 4(b) show that the polarization in the transition region between the classical $90°$ closure domain pattern has extremely small magnitude At an even higher value of $\theta = 51°$, we find that p has changed direction[1]. We compare Figs. 3(b), 4(a) for $\theta = 37°$ with Figs. 3(d), 4(c) for $\theta = 51°$. In the latter, there is no longer a simple transition to the free surface; instead there is a circular "vortex"-like structure with an anti-clockwise sense, and the direction of polarization at the surface is anti-parallel to that observed for $\theta = 37°$. The polarization magnitudes within this circular region are however quite small. We also note the steady increase in the stress and electric potential fields, Figs. 5, 6.

5   Effect of Surface Modulations

In this section, we examine the influence of periodic modulations of the free surface on closure domains microstructure. Figure 7 shows the profile of the free surface and also the corresponding triangle mesh with high density at the regions where microstructure is expected. The shape of the free surface is a sinusoid with the equation: $100 \sin(\pi x/400)$, based on the approach of [40]. To enable simpler calculations, [40] use a uniform finite difference mesh and approximate boundary conditions. The FEM / BEM that we have described above enables an accurate description of the free surface and also the calculation of fields outside the specimen.

Our initial condition for p with no lattice orientation and the entire surface is traction free. We use $\theta = 0$ to enable comparison to the simple $90°$ closure domains. Figure 8 shows the closure domains under the modulated surface. An important feature is that the peaks are better able to accommodate the competition between the surface (gradient) energy and the surface charges in comparison to the valleys. The gradient term drives p to transition smoothly while the electric field energy drives p to be normal to the surface. As the vector plot in Fig. 8 shows, it is possible to do both these things in the peaks unlike in the valleys. This contrast is also clearly visible in the stress field variations. A consequence is that surface modulations reduce the stray and interior electric fields by providing more options for the polarization to

---

[1]The crystal symmetry implies that $\theta = 51°$ and $\theta = 39°$ are equivalent. However, the initial condition that we use for the polarization enables a meaningful distinction in our calculations.

align itself tangential to the free surface

6   Effect of Far-Field Applied Stresses

We next examine the effect of moderate normal stress applied in the far-field along the horizontal direction, such as might be applied through substrate-thin film interactions. We focus on the influence of the applied stress, in conjunction with variation of θ, on the stray electric fields. We examine three values of applied stress: $\sigma_0 = 0$, $\sigma_0 = -0.4$ and $\sigma_0 = -0.8$ (recall from section 2 that the non-dimensionalized elastic moduli are $O(10^2)$). The first case, stress free, is simply that described above, and the others are applied compressive stress. In all cases, the domain microstructure appears similar to the stress-free case and the differences can be clearly seen in the electric field magnitudes.

A general trend that we see in Fig. 9 is that increased stress leads to an increase in the maximum magnitude (over space) of the stray electric field. We also notice that increasing θ leads to a steady increase in stray field magnitude until about $27°$. At this point, the transition closure domains nucleate and the electric field holds steady until about $37°$ when it again begins a steady increase. An interesting feature is that this trend is independent of stress level, though the specific magnitudes are different.

We also calculate an example of the interaction between applied stress and modulated surfaces. From Fig. 10, we notice that electric fields at modulated surfaces, with $\sigma_0 = -0.4$, are significantly smaller than those under flat surfaces with $\theta = 21°$. This suggests that modulated surfaces accommodate $\boldsymbol{p}$ better than flat surfaces and give rise to lower stray fields, even under applied stress when stress concentrations may have been expected to have an effect.

7   Effect of Far-Field Applied Electric Fields

The last case that we study is closure domain microstructure with different θ under far-field electric fields that are applied parallel to the free-surface. We study two values of applied field: -0.002 and -0.005, the negative sign indicating that they tend to cause $\boldsymbol{p}$ to point to the left. We recall from section 2 that the non-dimensionalized breakdown voltage (for the computational domain height) is $O(10)$.

We find that the structure of the closure domains very close to the free surface changes due to applied field. We focus on the particular case $\theta = 45°$, Fig. 12. For reference, we show again $\boldsymbol{p}$ without applied field in Fig. 12(a) and note that the triangular closure domains are roughly equal in both directions. Under applied field -0.002 that tends to align $\boldsymbol{p}$ to point to the left, Fig. 12(b), we find that the fraction of closure domains pointing in the preferred direction has grown at the expense of those pointing against the field. This is even more pronounced under applied field -0.005, Fig. 12(c), when the domain pointing against the field has almost vanished. This coupling between closure domain structure and applied field causes changes in the total electric fields not just along the applied field but also in the transverse direction.

The effect of applied field is also clearly seen in the electrostatic fields that are generated (Fig. 11). If we look away from the free surface where the potential is high in both cases, we see that the larger electric field causes a larger external and internal electric field, but also one that is more delocalized. As we did with applied stress, we also examine the interaction between orientation θ and applied field, Fig. 9. We note that the general trend remains that increased θ leads to increased external electric fields. However,

we find that the plateau between $27°$ and $37°$ is less pronounced. Interestingly, we find that an applied electric field of -0.002 has a smaller electric field magnitude than without applied field. This can be understood by noting that the applied electric field, unlike applied stress, breaks the left-right symmetry of the crystal: θ and $-\theta$ are physically different situations. In this case, the applied electric field cancels (to some extent) the electric field due to bound charges; in the case with $-\theta$ these electric fields would add up. We note that the applied electric field of -0.005 dominates the field due to bound charges, and hence the electric field magnitude is larger than without applied field.

8   Conclusions

We have applied a real space phase-field approach to calculate the domain microstructure beneath a ferroelectric free surface. We have investigated the influence of three parameters: first, the orientation of the free surface relative to the crystal directions; second, the effect of far-field applied normal stress; and third, the effect of far-field applied electric field. We have also examined the effect of surface modulations.

In general, the closure domain patterns are complex due to the competition between anisotropy energy, electrical energy and elastic energy. Some broad trends and conclusions emerge from our calculations. In the case of variation in surface orientation, we find that stray fields and stresses increase monotonically with increase in orientation angle, though there is a plateau during which the closure domain structure changes significantly. In the case of surface modulations, we find that providing a varying surface profile enables relatively low-energy domain structures with smaller stresses and electric fields compared to flat surfaces. The cause of this is that polarization can now be easily accommodated tangential to the free surface. However, we also observe an interesting contrast between the behavior of peaks and troughs, where the former lead to lower stresses due to allowing smoother changes in the field. We find that applied normal far-field stresses in general lead to higher stray electric fields, and also that the interaction between orientation and applied stress preserves the trends observed without applied stress. With applied electric fields, we observe the interesting cancellation between applied electric fields and those formed due to bound charges; when the magnitude of the applied fields is increased, they dominate and stray fields are larger than without applied field.

Stray fields at free surfaces have been experimentally observed, and are further being exploited [6, 7] as mentioned in the introduction. These and other works, e.g. scanning-probe microscopy measurements [41], show that periodic stray fields exist above the surface of a periodically-poled microstructure. These provide support for the possibility that charge compensation is incomplete at free surfaces and the existence of stray fields as we have calculated. However, these experimental efforts have focused on specimens with crystal axes oriented along the film surface. Our results for other orientations, as well as with applied fields, can enable experimental strategies to obtain stray fields of larger magnitude. We also mention analytical work [42, 43] that looks at stray fields in ferroelectrics; however, two important differences between those calculations and ours are that first, it is simplified to one dimension to enable analysis, and second, mobile charges are included in the analysis.

Among possible future questions of interest, we note two of particular importance. The first is to examine the effect of space charges. These are well-known to play an important role at domain walls and as well as free surfaces [42, 43]. Recent continuum field models for space charges [44] are readily integrated with our numerical approach to electrostatics. The second question is to examine the effect of surface

modulation on domain nucleation; this is of direct relevance to devices, e.g. thin-film switching. This has recently been examined by [40] using approximate boundary conditions and finite difference methods for simplicity. They find that the surface modulation act as sites for domain nucleation under applied fields. Due to the sensitive dependence of nucleation processes on inhomogeneities from geometry, it is important to study this question with a numerical method, such as presented here, that resolves the surface accurately.

Acknowledgment

A Electrostatic Greens Function in Two Dimensions with Periodicity in One Direction

We calculate an analytical expression for the Greens function in two dimensions assuming periodicity in a single direction following a general technique outlined in [45].

The fundamental solution of a single point source in 2-D at $\boldsymbol{x}$ is

$$G^0(\boldsymbol{x}, \boldsymbol{y}) = \log(|\boldsymbol{x} - \boldsymbol{y}|) \tag{A.1}$$

and the components of the electric field at $\boldsymbol{y}$ due to the point source at $\boldsymbol{x}$ are

$$
\begin{aligned}
E_1^0(\boldsymbol{x}, \boldsymbol{y}) &= \frac{\partial G^0}{\partial x_1} = \frac{x_1 - y_1}{(x_1 - y_1)^2 + (x_2 - y_2)^2} \\
E_2^0(\boldsymbol{x}, \boldsymbol{y}) &= \frac{\partial G^0}{\partial x_2} = \frac{x_2 - y_2}{(x_1 - y_1)^2 + (x_2 - y_2)^2}
\end{aligned}
\tag{A.2}
$$

To obtain the Greens function for a periodic array of charges, we superpose the fields from charges located at integer multiples of the periodicity L in the $\boldsymbol{e}_1$ direction:

$$G(\boldsymbol{x}, \boldsymbol{y}) = \sum_{n=-\infty}^{n=+\infty} \log(|\boldsymbol{x} + nL\boldsymbol{e}_1 - \boldsymbol{y}|) \tag{A.3}$$

This sum is not convergent. Hence we work directly with the electric field:

$$
\begin{aligned}
E_1(\boldsymbol{x}, \boldsymbol{y}) &= \sum_{n=-\infty}^{n=+\infty} \frac{x_1 + nL - y_1}{(x_1 + nL - y_1)^2 + (x_2 - y_2)^2} \\
E_2(\boldsymbol{x}, \boldsymbol{y}) &= \sum_{n=-\infty}^{n=+\infty} \frac{x_2 - y_2}{(x_1 + nL - y_1)^2 + (x_2 - y_2)^2}
\end{aligned}
\tag{A.4}
$$

The component E_1 is conditionally convergent but E_2 is absolutely convergent and is evaluated to be:

$$E_2 = \frac{\pi}{L} \frac{\cosh\left(\pi \frac{x_2 - y_2}{L}\right) \sinh\left(\pi \frac{x_2 - y_2}{L}\right)}{\cosh^2\left(\pi \frac{x_2 - y_2}{L}\right) - \cos^2\left(\pi \frac{x_1 - y_1}{L}\right)} \tag{A.5}$$

We can integrate this to obtain the desired Green's function:

$$G = \frac{1}{2} \log\left(\cosh^2\left(\pi \frac{x_2 - y_2}{L}\right) - \cos^2\left(\pi \frac{x_1 - y_1}{L}\right)\right) \tag{A.6}$$

References

[1] Y. Xu. *Ferroelectric materials and their applications*. North-Holland, 1991.

[2] K. Uchino. *Piezoelectric Actuators and Ultrasonic Motors*. Kluwer, 1996.

[3] J.F. Scott. *Ferroelectric memories*. Springer Verlag, 2000.

[4] A. K. Tagantsev, V. O. Sherman, K. F. Astafiev, J. Venkatesh, and N. Setter. *J. Electroceram.*, 11:5–66, 2003.

[5] K. Dayal and K. Bhattacharya. *J. Appl. Phys.*, 102:064102, 2007.

[6] N.V. Burbure, P.A. Salvador, and G.S. Rohrer. *Journal of the American Ceramic Society*, 89(9):2943–2945, 2006.

[7] D. Li and D.A. Bonnell. *Annual Review of Materials Research*, 38(1):351, 2008.

[8] B.W. Wessels. *Annual Review of Materials Research*, 37(1):659, 2007.

[9] K. Dayal and K. Bhattacharya. *Acta Mater.*, 55:1907–1917, 2007.

[10] L. Yang and K. Dayal. *J. Comput. Phys.*, submitted.

[11] N. Sai, A.M. Kolpak, and A.M. Rappe. *Physical Review B*, 72(2):020101, 2005.

[12] T. Nishimatsu, U.V. Waghmare, Y. Kawazoe, and D. Vanderbilt. *Physical Review B*, 78(10):104104, 2008.

[13] B.K. Lai, I. Ponomareva, II Naumov, I. Kornev, H. Fu, L. Bellaiche, and GJ Salamo. *Physical review letters*, 96(13):137602, 2006.

[14] B.K. Lai, I. Ponomareva, I. Kornev, L. Bellaiche, and G. Salamo. *Applied Physics Letters*, 91:152909, 2007.

[15] L.Q. Chen. *Journal of the American Ceramic Society*, 91(6):1835–1844, 2008.

[16] L.Q. Chen. *Annual Review of Materials Research*, 32(1):113–140, 2002.

[17] YL Li, SY Hu, ZK Liu, and LQ Chen. *Acta materialia*, 50(2):395–411, 2002.

[18] D.G. Schlom, L.Q. Chen, C.B. Eom, K.M. Rabe, S.K. Streiffer, and J.M. Triscone. *Annu. Rev. Mater. Res.*, 37:589–626, 2007.

[19] YL Li, S. Choudhury, ZK Liu, and LQ Chen. *Applied physics letters*, 83(8):1608–1610, 2003.

[20] SY Hu, YL Li, and LQ Chen. *Journal of applied physics*, 94(4):2542–2547, 2003.

[21] YL Li, SY Hu, ZK Liu, and LQ Chen. *Applied physics letters*, 81:427, 2002.

[22] Y. Jiang, Y. Zhang, B. Liu, and D. Fang. *Acta Materialia*, 57(5):1630–1638, 2009.

[23] D. Fang, Y. Jiang, S. Li, and CT Sun. *Acta Materialia*, 55(17):5758–5767, 2007.

[24] D. Fang and J. Li. in preparation.

[25] A. Abdollahi and I. Arias. *Acta Materialia*, 59:4733, 2011.

[26] J. Wang and T. Y. Zhang. *Acta Materialia*, 55:2465, 2007.

[27] Y. C. Song and A. K. Soh and Y. Ni. *Journal of Physics D: Applied Physics*, 40:1175, 2007.

[28] JM Adams and M. Warner. *Physical Review E*, 79(6):61704, 2009.

[29] Y. C. Shu and K. Bhattacharya. *Philos. Mag. B*, 81:2021–2054, 2001.

[30] W. Zhang and K. Bhattacharya. *Acta Mater.*, 53:185–198, 2005.

[31] YC Shu, JH Yen, HZ Chen, JY Li, and LJ Li. *Applied Physics Letters*, 92:052909, 2008.

[32] LJ Li, JY Li, YC Shu, and JH Yen. *Applied Physics Letters*, 93:192506, 2008.

[33] M. Y. El-Naggar, K. Dayal, D. G. Goodwin, and K. Bhattacharya. *J. Appl. Phys.*, 100:114115, 2006.

[34] Y. Su and C.M. Landis. *Journal of the Mechanics and Physics of Solids*, 55(2):280–305, 2007.

[35] M. Porta, T. Lookman, and A. Saxena. *Journal of Physics: Condensed Matter*, 22:345902, 2010.

[36] D. Schrade, R. Mueller, BX Xu, and D. Gross. *Computer methods in applied mechanics and engineering*, 196(41-44):4365–4374, 2007.

[37] A. Artemev, B. Geddes, J. Slutsker, and A. Roytburd. *Journal of Applied Physics*, 103:074104, 2008.

[38] J. Wang, M. Kamlah, T.Y. Zhang, Y. Li, and L.Q. Chen. *Applied physics letters*, 92:162905, 2008.

[39] W.F. Rao, T.L. Cheng, and Y.U. Wang. *Applied Physics Letters*, 96:122903, 2010.

[40] R. Ahluwalia, N. Ng, and D.J. Srolovitz. *Nanotechnology*, 20:445709, 2009.

[41] M. Shvebelman, P. Urenski, R. Shikler, G. Rosenman, Y. Rosenwaks, and M. Molotskii. *Applied physics letters*, 80:1806, 2002.

[42] Y. Watanabe. *Physical Review B*, 57(2):789, 1998.

[43] Y. Watanabe, M. Okano, and A. Masuda. *Physical Review Letters*, 86(2):332–335, 2001.

[44] Y. Xiao and K. Bhattacharya. *Arch. Rat. Mech. Anal.*, 189(1):59–95, 2008.

[45] J. Kevorkian. *Partial differential equations: analytical solution techniques*. Springer Verlag, 2000.

[46] M.A. Heald and J.B. Marion. *Classical electromagnetic radiation*. Brooks/Cole Publishing, 1995.

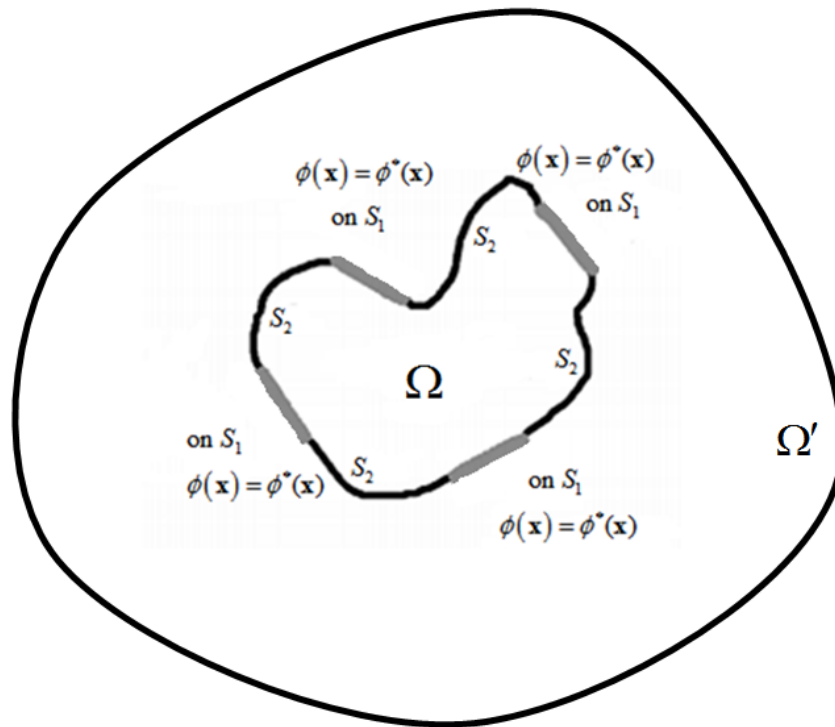[47] L Q Chen and J Shen. *Computer Physics Communications*, 108:147, 1998.

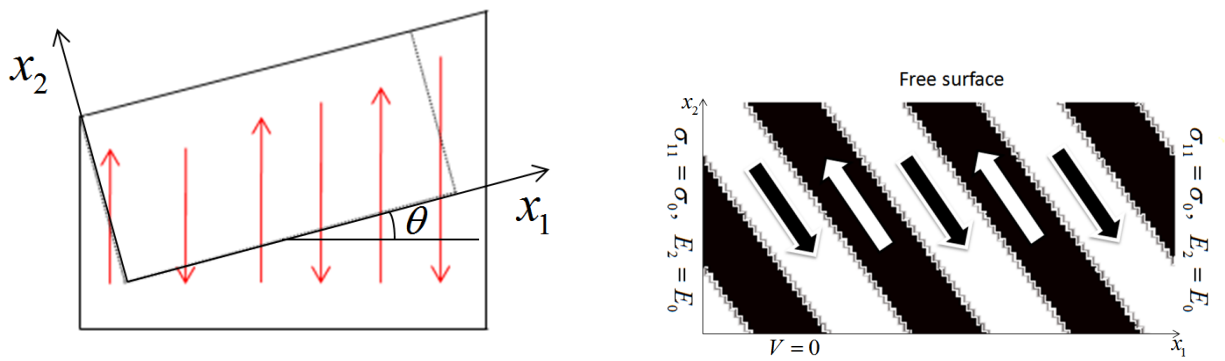Figure 1: Domain and boundary condition for electrostatics problem.

Figure 2: Computational domain: (left) orientation relative to crystal axes; (right) boundary conditions.

(a) $\theta = 14°$.

(b) $\theta = 37°$.

(c) $\theta = 45°$.

(d) $\theta = 51°$.
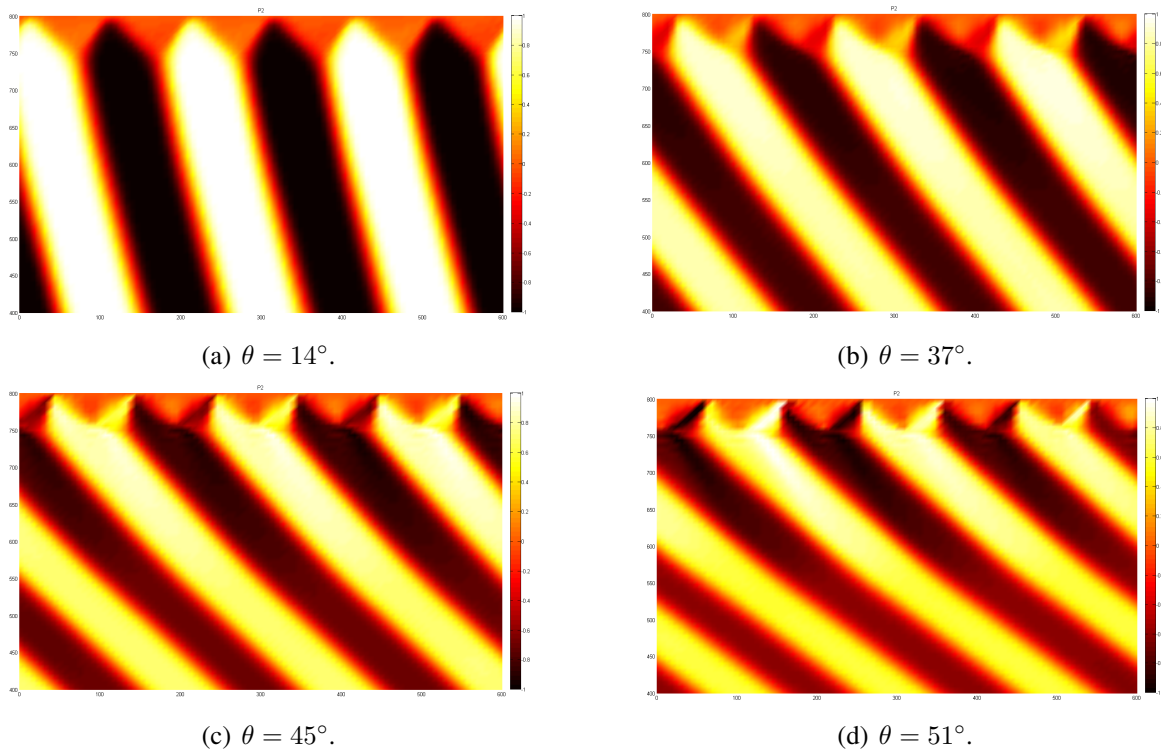
Figure 3: Closure domains (vertical component of p) with different orientations θ in the absence of applied far-field stress and electric field.

(a) $\theta = 37°$.

(b) $\theta = 45°$.

(c) $\theta = 51°$.
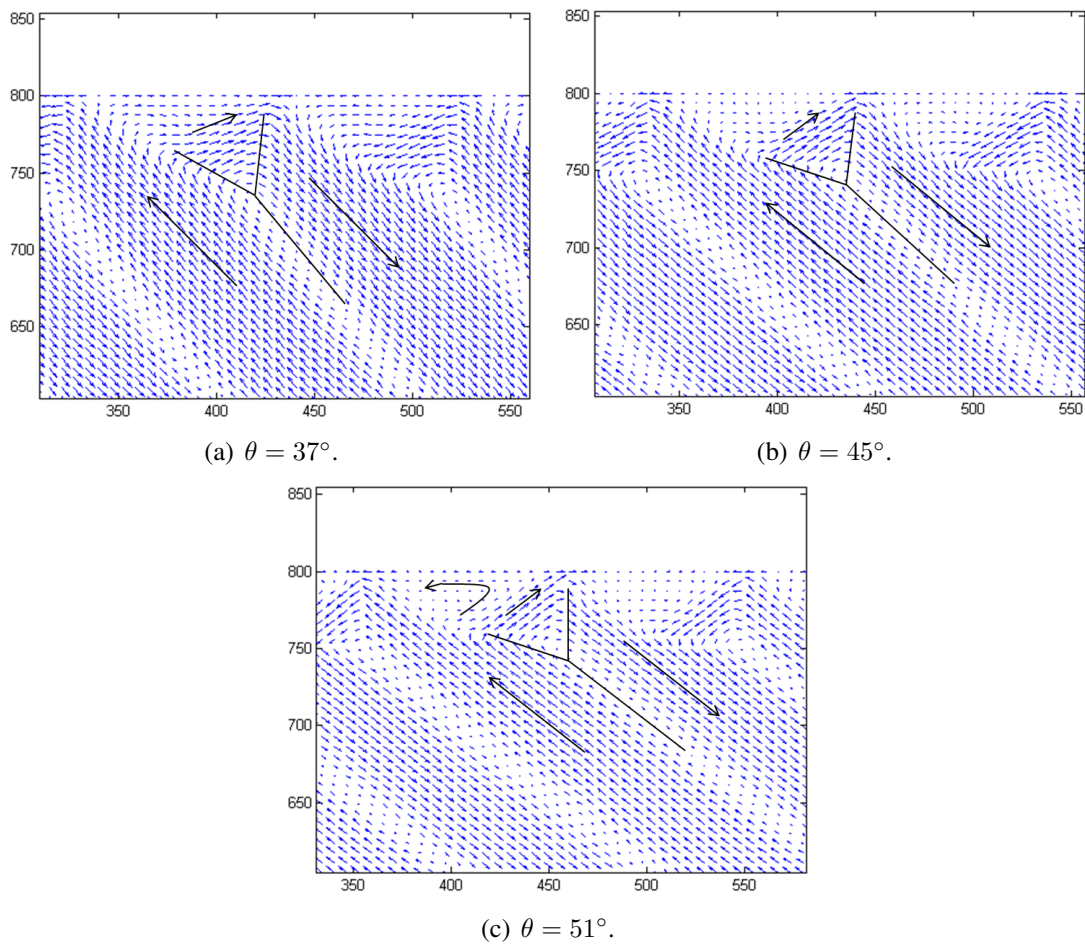
Figure 4: Detail view of closure domains (vector plot of $\boldsymbol{p}$) in the absence of applied far-field stress and electric field with different orientations θ.
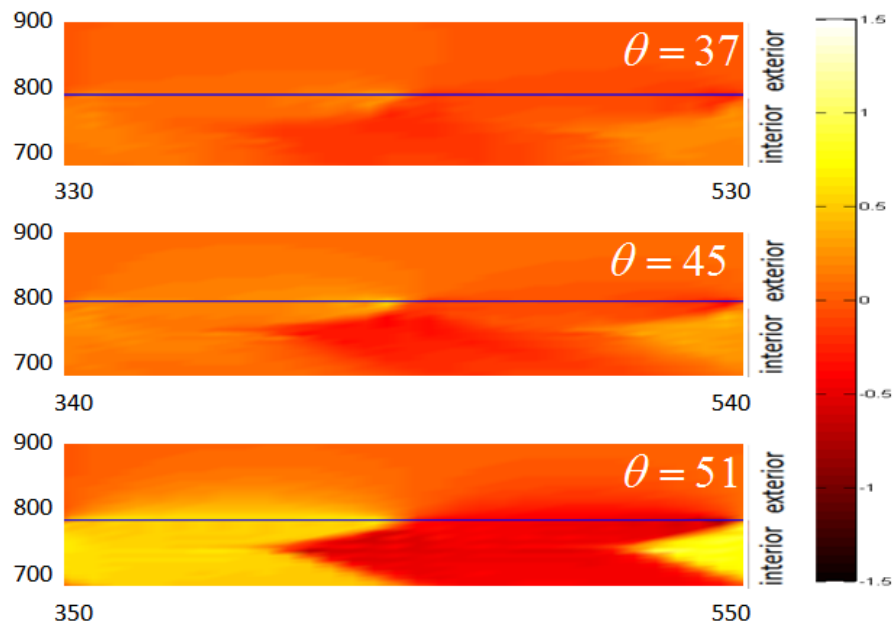
Figure 5: Electrostatic potential in the vicinity of closure domains for different orientations θ.

15
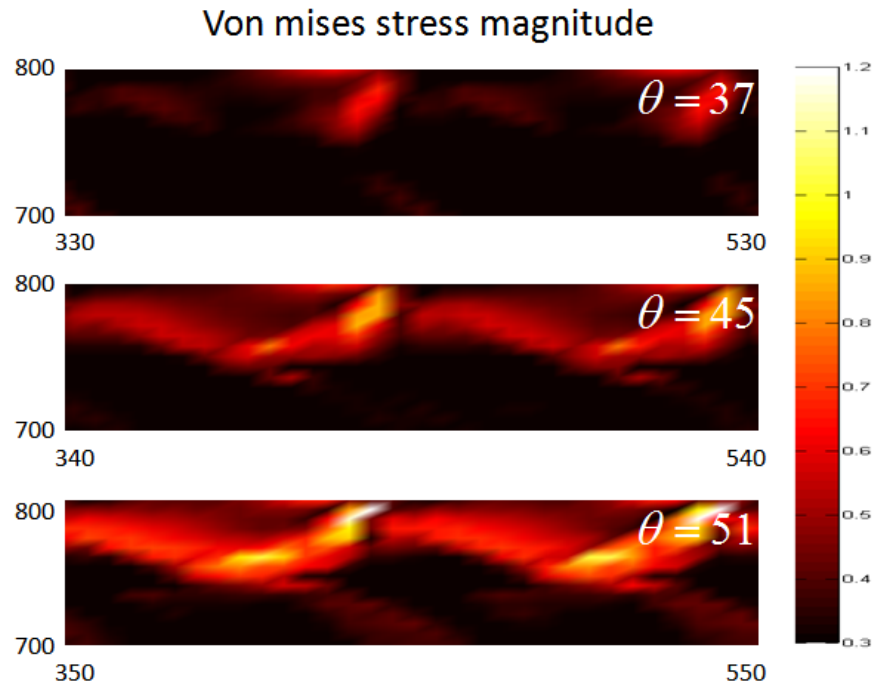
Figure 6: Von Mises stress in the vicinity of closure domains for different orientations θ.
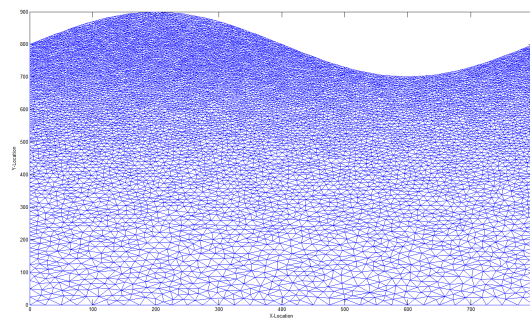
Figure 7: Surface modulation profile and unstructured fine mesh at the free surface.
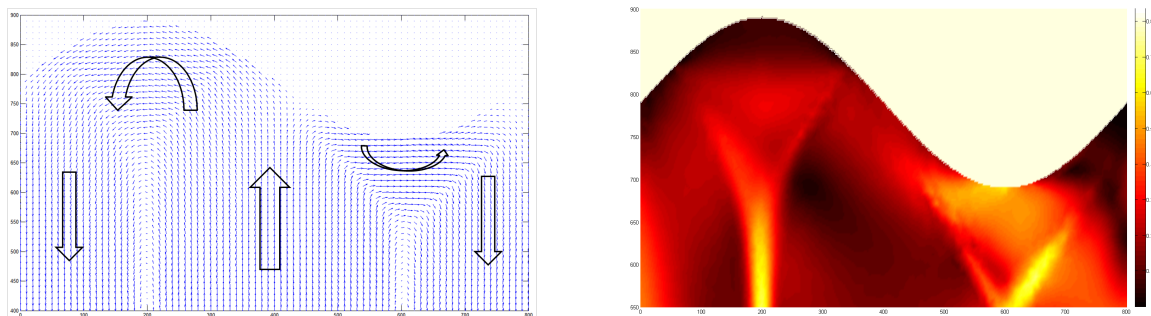
Figure 8: Closure domains under sinusoidal surface with $\theta = 0$: (left) polarization; (right) Von Mises stress
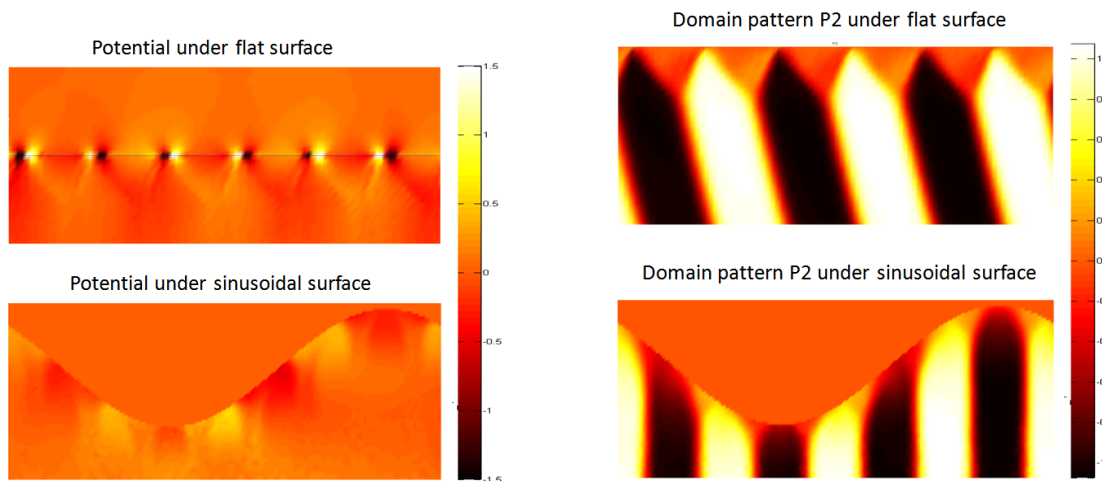
16
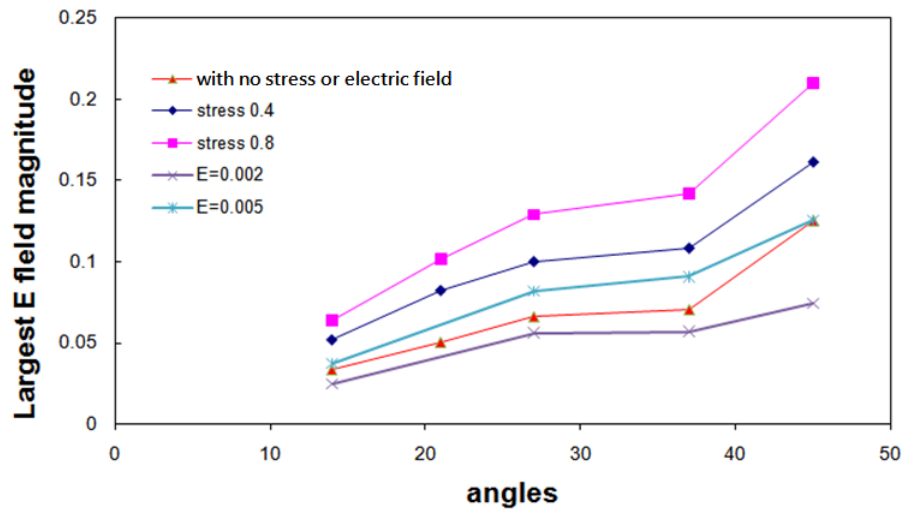
Figure 9: Maximum (over space) of the magnitude of electric field as a function of θ for different applied far-field stress and applied electric field.

(a) Polarization and electric potential at a flat surface with $\theta = 21°$.

(b) Polarization and electric potential at modulated surface with $\theta = 0°$.

Figure 10: Electrostatic potential and p for flat surface ($\theta = 21°$) and modulated surface with applied stress $\sigma_0 = -0.4$.
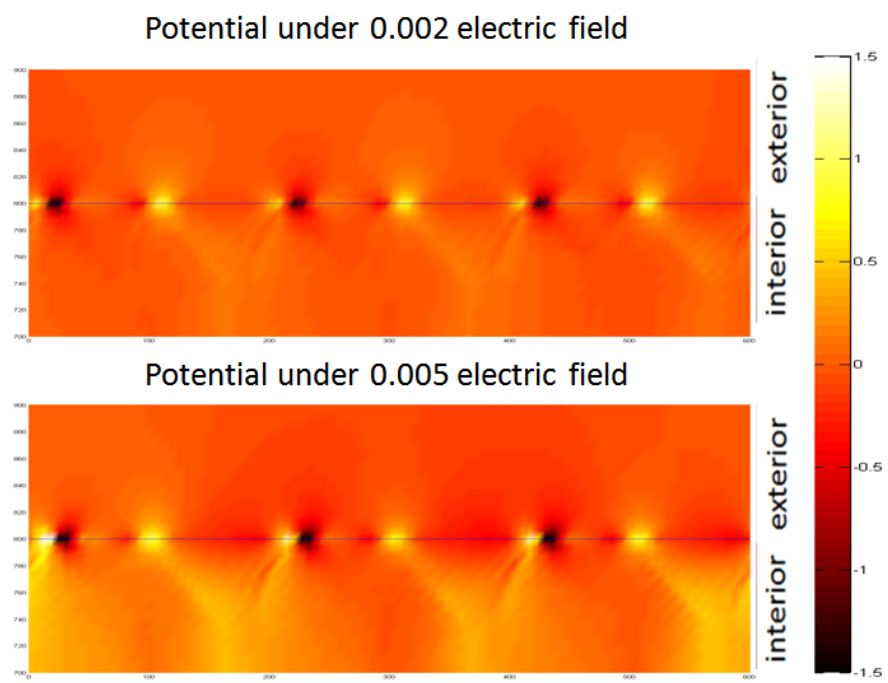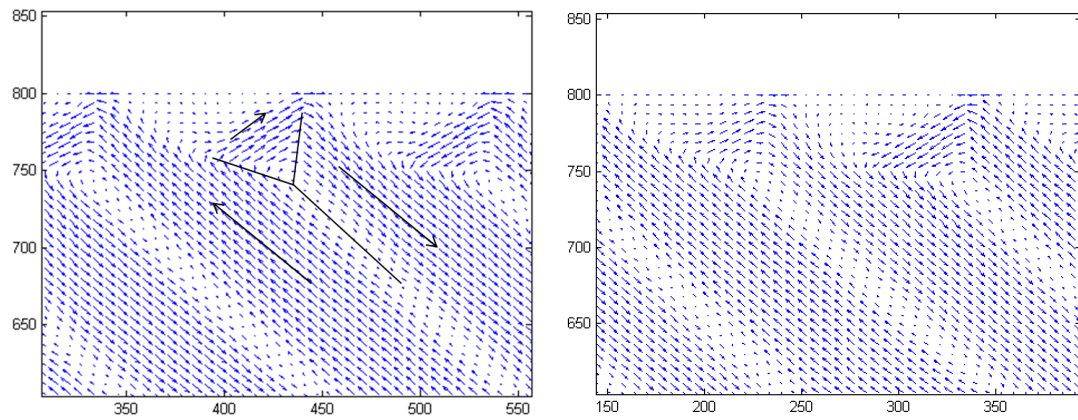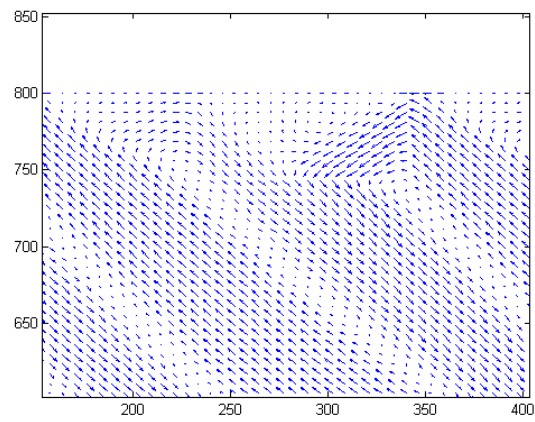
Figure 11: Change in electrostatic potential due to applied electric fields.

(a) Polarization field of closure domain with 45 degree lattice orientation under free electric field.

(b) Polarization field of closure domain with 45 degree lattice orientation under 0.002 electric field.

(c) Polarization field of closure domain with 45 degree lattice orientation under 0.005 electric field.

Figure 12: Polarization field ($\theta = 45°$) with different applied electric fields.